Journal of Power Sources 269 (2014) 54–60

Contents lists available at ScienceDirect

Journal of Power Sources

journal homepage: www.elsevier.com/locate/jpowsour

Lysine-derived mesoporous carbon nanotubes as a proficient non-precious catalyst for oxygen reduction reaction

Rongfang Wang [a, *], Tianbao Zhou [a], Hui Wang [a], Hanqing Feng [b], Shan Ji [c, 1]

[a] College of Chemistry and Chemical Engineering, Northwest Normal University, Lanzhou 730070, China
[b] College of Life Science, Northwest Normal University, Lanzhou 730070, China
[c] South African Institute for Advanced Materials Chemistry, University of the Western Cape, Cape Town 7535, South Africa

HIGHLIGHTS

- Porous carbon nanotubes with a diameter of ca. 300–400 nm (LPCNs) derived from lysine.
- LPCNs exhibit higher activity than Pt/C (20 wt%) for oxygen reduction reaction (ORR).
- LPCNs show higher stability for ORR and tolerance for methanol than Pt/C (20 wt%).
- The superior performance of LPCNs results from the unique structure and the doped effect.

GRAPHICAL ABSTRACT

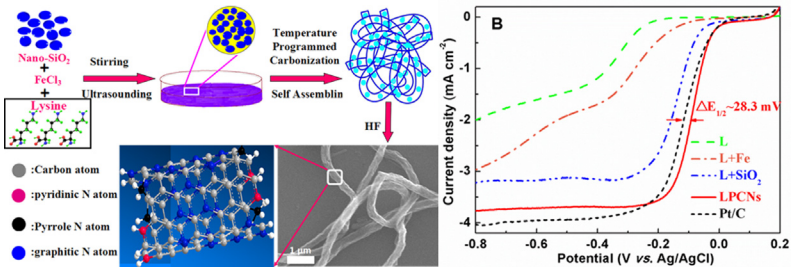

ARTICLE INFO

Article history:
Received 5 March 2014
Received in revised form
27 June 2014
Accepted 27 June 2014
Available online 7 July 2014

Keywords:
Oxygen reduction reaction
Catalyst
Carbon nanotube
N-doped
Mesopore

ABSTRACT

N-doped carbon nanotubes are highly favored for use as electrocatalysts for oxygen reduction reaction (ORR) because of their relatively low cost and superior catalytic activity. Here, Lysine-derived porous carbon nanotubes (LPCNs) with large inner cavities of ca. 300–400 nm are reported as electrocatalyst for ORR. LPCNs exhibit 28.3 mV of more positive half-wave-potential than that of commercial Pt/C. In addition, LPCNs is much more stable and tolerant to fuel crossover effect than Pt/C. The above superiorities make it a promising candidate for substituting noble metal catalysts as a cathode catalyst for ORR.

1. Introduction

The cathodic oxygen reduction reaction (ORR) plays a crucial role in electrochemical energy conversion in fuel cells [1]. Pt-based materials have long been regarded as active catalysts for ORR [2]; however, these noble metal catalysts hinder to mass market fuel cells for commercial application due to their high cost, sluggish electron transfer kinetics, and limited supply [3]. Along with recent intensive research efforts in reducing or replacing Pt-based catalyst, a suitable substitute for Pt-based catalysts, nitrogen-doped carbon nanotubes were reported to exhibit excellent electrocatalytic performance for ORR [4]. Compared to commercially available Pt-based catalysts, these nitrogen-doped carbon nanotubes possess the advantages of low cost, excellent electrocatalytic activity, free from CO poisoning, fuel crossover effect and long durability [5]. The

* Corresponding author. Tel./fax: +86 931 7971533.
E-mail addresses: wangrf@nwnu.edu.cn, wrf38745779@126.com (R. Wang), sji@uwc.ac.za (S. Ji).
[1] Tel./fax: +27 21 9599316.

http://dx.doi.org/10.1016/j.jpowsour.2014.06.156
0378-7753/

enhanced electrochemical performance of nitrogen-doped carbon nanotubes toward ORR could be attributed to two sides; one is the well-defined high surface area which introduces spacing for improved electrokinetics, as well as good electrical and mechanical properties. Another is the electro-accepting ability of nitrogen species, which creates net positive charges on adjacent carbon atoms to facilitate oxygen adsorption for ORR with low overpotential [6].

The approach for the synthesis of nitrogen-doped nanotubes commonly used is chemical vapor deposition (CVD) [4,6,7], which employs liquid organic molecules as a carbon source to synthesize nanotubes on the base material via rearranging the carbon and nitrogen atoms on the metal catalysts at high temperatures [8,9]. In this case, the drawbacks are the use of expensive precursors and rigorous conditions or special instruments required [10]. In addition, some nitrogen precursors, such as NH_3 [11] used in the CVD process, are toxic, and careful treatments are essential, which may limit the practical application of these gas-phase synthesis methods. Therefore, creating nitrogen-doped nanotubes catalysts entirely derived from abundant, non-toxic precursors by a facile approach are of great importance for fuel cells.

On the other hand, a nanoporous structure with large surface area is highly desirable for electrochemical activity of these promising nanotubes. Efforts to construct nanoporous structure along with large surface area usually involve the templating approaches. Yang et al. prepared mesoporous nitrogen-doped carbon materials with high surface areas up to 1500 $m^2\ g^{-1}$ by using SiO_2 nanoparticles as hard templates [12]. A three-dimensionally ordered macroporous graphitic C_3N_4/carbon composite was fabricated by using SiO_2 nanoparticles for mesostructure control [13]. In our previous work [14], lysine-derived nitrogen-doped porous nanotubes (LPCNs) using SiO_2 nanoparticles as the template were prepared, which have rugged wall and much larger diameter than other reports, thus, have large specific surface area. In this work, the resultant LPCNs were demonstrated to show superior electrocatalytic activities compared to commercial Pt/C due to the formation of the unique architecture and synergic effect from Fe and N.

2. Experimental

2.1. Chemicals and materials

Lysine (Lys) was purchased from Shanghai Kangda Amino Acid Factory. Silicon dioxide (SiO_2, ca. 30 ± 15 nm) was purchased from Aladdin. Ferric chloride hexahydrate ($FeCl_3 \cdot 6H_2O$) was purchased from Yantai Shuangshuang Chemical Co., Ltd. All chemical reagents used in this experiment were of analytical grade and used without further purification. Deionized water was used in all of experiment (≥18 MΩ).

2.2. Preparation of lysine-derived porous carbon nanotubes (LPCNs)

To prepare LPCNs, 2 g lysine were dissolved into $FeCl_3$ methanol/water solution ($V_{methanol}$:V_{water} = 2:1) with stirring magnetically. Subsequently, the mixed solution was ultrasonicated for 1 h at room temperature. Then, 426 mg SiO_2 nanoparticles were added to the mixture under ambient conditions stirred and ultrasonicated for 2 h to obtain a homogeneous mixture and was dried at 80 °C in blast oven for overnight. The mass ratio of the lysine, $FeCl_3 \cdot 6H_2O$, and SiO_2 was about 20:4:1. The resulting powder of mixture were heated to 300 °C maintained for 1 h under nitrogen atmosphere in a tubular furnace. Then the mixtures was continuously heated under nitrogen flow at 5 °C min^{-1} to 900 °C and kept there for 1 h; and finally cooled down to room temperature. In order to remove SiO_2 template, the powders were treated according to the following SiO_2 template removal procedure: stirring of dispersion into HF (20 wt%, 6 mL) solution for 1 day with stirring magnetically at room temperature, washing 10 times with water, centrifugation to recover the powders. Finally, the products were dried at 60 °C overnight to obtaine LPCNs catalyst.

In order to study the effect of doped $FeCl_3 \cdot 6H_2O$, and SiO_2, carbon materials derived from lysine, lysine + $FeCl_3 \cdot 6H_2O$, and lysine + SiO_2, respectively, were prepared by the same process. The resultant products were denoted as L, L + Fe, and L + SiO_2, respectively.

2.3. Characterization

TG-DSC was performed with a TG/DSC-1 instrument system (Mettler Toledo, Swiss). Samples were put in a 70 μL aluminium crucible with a programmed heating rate of 10 °C min^{-1} from room temperature to 1000 °C under nitrogen atmosphere. Element analysis was performed by an Organic Elemental Analyzer, Thermo Flash 2000. XPS was obtained by a VGEscalab210 spectrometer fitted with Mg 300 W X-ray source (England). Scanning electron microscope (SEM) measurements were carried out on a Carl Zeiss Ultra Plus (Germany). Transmission electron microscopy (TEM) measurements were carried out on a JEM-2010 Electron Microscope (Japan) with the acceleration voltage of 200 kV. Raman spectroscopy measurements were carried out on a Ft-Raman spectroscopy (RFS 100, BRU-KER) employing Nd: YAG laser wavelength of 1064 nm. The sorption isotherm was carried out on Quantachrome Autosorb-1 volumetric analyzer.

2.4. Electrochemical measurements

The electrochemical measurement was evaluated on an electrochemical work station (CHI650). A conventional constant temperature three-electrode cell was used, including an Ag/AgCl (saturated KCl solution) electrode as the reference electrode, a platinum wire as the counter electrode, and Rotating disk electrode (RDE, 5 mm in diameter, 0.196 cm^2) as the working electrode. The thin-film electrode was prepared as follows: 5 mg of catalyst was dispersed ultrasonically in 1 mL Nafion/ethanol (0.25% Nafion) for 5 min. 8 μL suspensions dropped on the surface of the glassy carbon rotating disk electrode, followed by drying in air at room temperature. The loading of catalysts is ca. 20.4 mg cm^{-2}. Before each measurement, the electrolyte, 0.1 mol L^{-1} KOH solution, was purged with high-purity N_2 or O_2 gas for at least 15 min to ensure the gas saturated. All test temperature was controlled to 30 °C.

3. Results and discussion

As shown in Scheme 1, the synthesis of LPCNs involves a programmed thermal reaction to yield SiO_2 nanoparticles inserted Fe, N-doped carbon nanotubes, and then HF acid leaching of SiO_2 nanoparticles and soluble Fe species. The chemical reaction during pyrolysis of the lysine, SiO_2, and $FeCl_3 \cdot 6H_2O$ composite was studied by thermogravimetric-differential scanning calorimetry analysis (TG-DSC) analysis, which is shown as Figure S1 (Supporting Information). From the data, it can be observed that the formation of LPCNs involves two steps, e.g. decomposition and self-assembly processes, as shown in Scheme 1.

The morphology of LPCNs was observed by scanning electron microscope (SEM) and transmission electron microscopy (TEM) techniques (Fig. 1). As can be seen from Fig. 1A, LPCNs exhibit the morphology of open-ended, curved tube with the additional presence of some carbon debris. However, a few bright points are

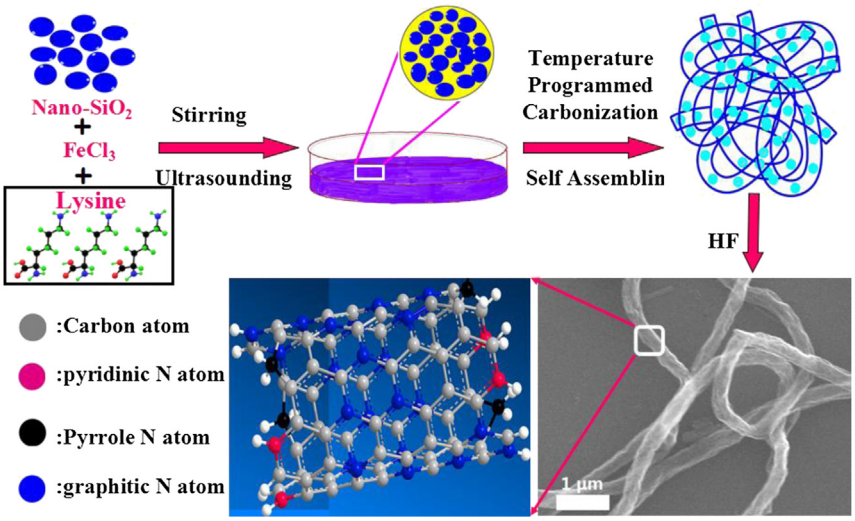

Scheme 1. Schematic routes showing the preparation of LPCNs by self assembly and temperature programmed.

observed which could be related to the particles of SiO_2 or Fe species during the thermal treatment. Fig. 1B and C shows TEM image of different parts of LPCNs. The TEM image of LPCNs in Fig. 1B shows that its surface appears to be composed of individual graphite sheets stacked together to form a wrinkled layer, which is different to the straight cylindrical geometry of common carbon nanotubes reported by other groups [9,10,15,16]. The outer diameter, inner cavities, of the tubes is estimated to be between ~300 and 400 nm. In some reports [6,11,17,18], the outer diameter of the prepared nanotubes is ca. 50 nm, which is significantly lower than that of LPCNs. Here, black spots, the particle of SiO_2 or Fe species are also visible, and that these particles being encapsulated by carbon layers were protected from the HF treatment. Besides, carbon debris, e.g. graphene sheets which is residue during the formation of LPCNs, is also visible in Fig. 1B. The high magnification view of the tube's end shown in Fig. 1C clearly reveals stacks of graphite sheets resulting in uneven end of the tubes. The HRTEM image in Fig. 1D display well-defined (002) lattice fringes staggered, further indicating stacks of graphite sheets. The EDX spectrum of LPCNs shown as the inset in Fig. 1C identifies the presence of C, N, O, Si and Fe elements. The bulk composition of LPCNs was evaluated by elemental analysis, and it found N at 6.9 wt%, C at 87.5 wt% and residue of SiO_2 and elemental Fe.

As is well known, Raman spectroscopy is a widely used technique to characterize the structural and electronic properties of carbon materials including disorder and degree of structural defect. Fig. 2A presents Raman spectrum of LPCNs. For comparison, Raman spectrum of the carbon (Vulcan XC-72) is also presented. As can be seen, both samples exhibit two peaks; one centered at ca. 1300 cm^{-1}, e.g. D band, is disorder induced. Another located at 1600 cm^{-1}, e.g. G band, is commonly observed for all graphitic structures and attributed to the E_{2g} vibrational mode present in the sp^2 bonded graphitic carbons [19]. The results demonstrate the formation of graphite structure for LPCNs, which is further

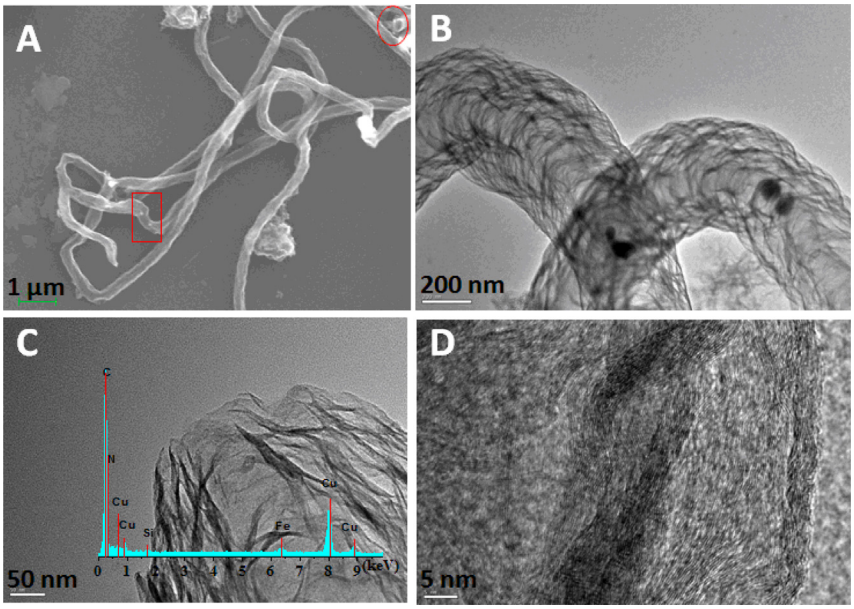

Fig. 1. (A) SEM image; (B, C) TEM images; (D) HRTEM image of LPCNs.

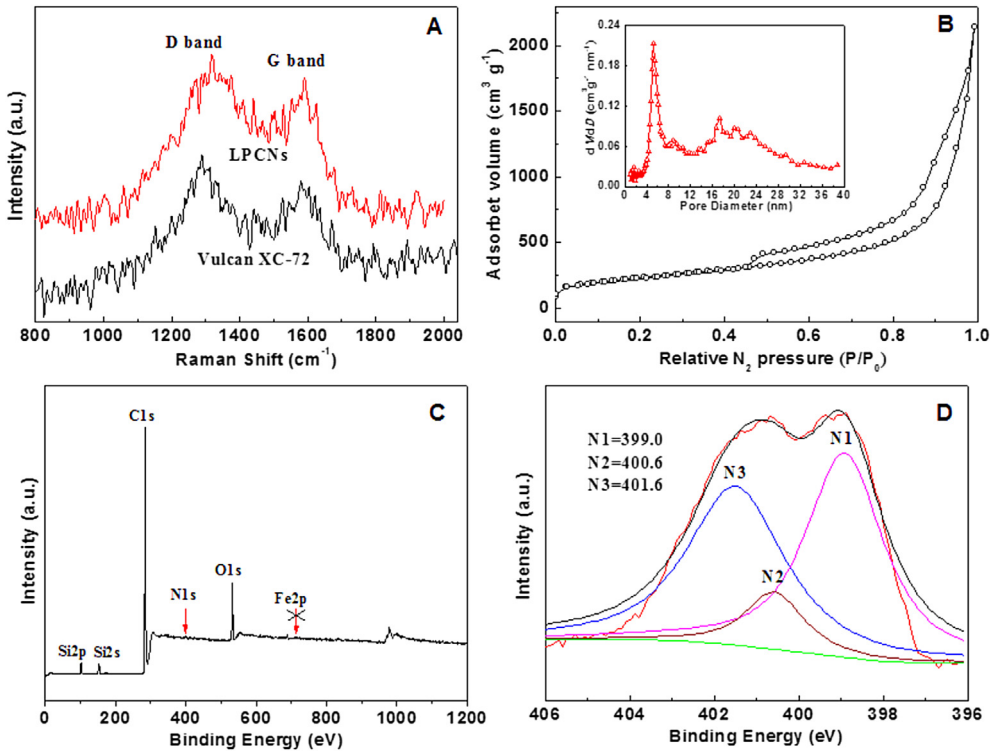

Fig. 2. (A) Raman spectra of LPCNs and Vulcan XC-72; (B) The nitrogen adsorption/desorption isotherms of LPCNs, inset: the diagram of pore diameter distribution; (C) XPS survey spectrum of LPCNs; and (D) The high resolution N 1s XPS spectrum of LPCNs.

confirmed by XRD pattern shown as Figure S2 (Supporting Information). Compared to D band of Vulcan carbon (~1296 cm^{-1}), D band of the prepared LPCNs is up-shifted to 1340 cm^{-1}. This phenomenon arising from nitrogen incorporated into carbon is similar to the results of nitrogen-doped carbon [20,21]. In addition, LPCNs is found to have 1.12 of I_D/I_G ratio, obviously lower than 1.23 observed for Vulcan carbon, which is a result of the higher amount of sp^2 carbon. The high amount of sp^2 carbon of LPCNs would improve its electron conductivity, which can facilitate the electrons transfer occurring in chemical reactions [22].

The porous property of LPCNs was investigated by isotherms of adsorption–desorption of N_2 at 77 K. As shown in Fig. 2B, the nitrogen adsorption/desorption isotherms of LPCNs reveal a hybrid I/IV isotherm according to the international union of pure and applied chemistry (IUPAC) classification, indicative of the presence of two kinds of pores, micropores and mesopores, in LPCNs [23]. A distinct hysteresis loop is observed in the P/P_0 range of 0.4–0.85, indicating the presence of a large fraction of mesopores [24]. The inset in Fig. 2B shows the pore size distribution of LPCNs derived from DFT method, which exhibits LPCNs having a broad range of pore size distribution from ca. 1.0–39.0 nm. In which there are four clear peaks, centering at ca. 5.4, 17.3, 20.3 and 23.0 nm, in the mesopore range, indicating the mesoporous structure of LPCNs. Its BET surface area was measured to be 807.6 $m^2\ g^{-1}$ listed in Table S1, and much larger than those of as-prepared samples whose porous structure is shown as Figure S3. The unique structural feature and the mesoporous structure are more easily accessible to gaseous activation molecules than those of the conventional carbons, resulting in more efficient activation processes.

The surface composition and elemental chemical state of LPCNs were probed by X-ray photoelectron spectroscopy (XPS). As can be seen in Fig. 2C, the XPS survey spectrum of LPCNs shows a predominant narrow graphitic C 1s peak at 284.2 eV, along with an N 1s peak at *ca.*400.0 eV, an O 1s peak at ca. 532.1 eV, a Si 2p peak at ca. 101.9 eV, and a Si 2s peak at ca. 152.7 eV. While, any Fe signal doesn't appear, which is also confirmed by high resolution Fe 2p XPS spectrum (see Figure S4 in Supporting Information), indicating that Fe element existed in shallow layers in LPCNs is removed during the process of HF treatment.

The fitted high resolution N 1s XPS spectrum given in Fig. 2D reveals the presence of three types of N species, which are assigned to N1, pyridinic-N (BE = 399.0 eV) bonded to two carbon atoms at the edge of graphene planes, which donates one p-electron to the aromatic π system; N2, pyrrolic-N (BE = 400.6 eV) bonded to two carbon atoms and one H atom which contribute to the π system with two p-electrons; and N3, quaternary-N (BE = 401.6 eV) bonded to three C atoms is incorporated into the graphene layer and replaces carbon atoms within a graphene plane. Therefore, from the fitted results of the N 1s spectrum, N atoms not only incorporate into the graphene layer but also form a variety of functional groups, in which both N1 and N2 play roles in the ORR process. The N/C atomic ratio is calculated to be ca. 6.9%, which is higher than that of the N-doped carbon nanotubes used for ORR study in work of Dai's group [25].

We performed the rotating ring electrode (RDE) cyclic voltammograms (CVs) to investigate electrocatalytic activities of LPCNs for ORR in N_2 or O_2-saturated 0.1 mol L^{-1} KOH electrolyte. Shown in Fig. 3A, a substantial reduction process occurs at about 0.18 V in the presence of oxygen, whereas no obvious response is observed at the same potential range under nitrogen, indicating LPCNs have catalytic activity for ORR. Linear sweep voltammograms (LSV) can provide further insight into the catalytic activity of LPCNs. To prove the doped effect of $FeCl_3 \bullet 6H_2O$ and SiO_2 template in ORR electrochemical process, Fig. 3B compares the LSVs at different electrodes including LPCNs, L, L + Fe, L + SiO_2, and commercial Pt/C. At a

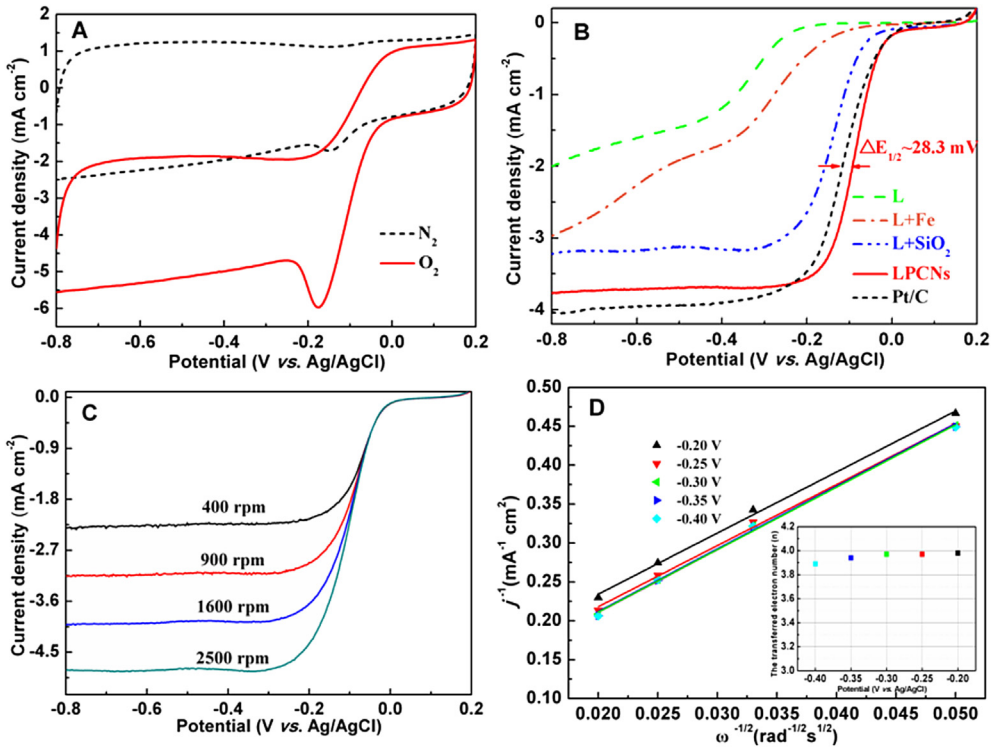

Fig. 3. (A) CVs of LPCNs in N_2/O_2-saturated 0.1 mol L^{-1} KOH solution at a scan rate of 5 mV s^{-1} and rotation rate of 1600 rpm. (B) LSVs of LPCNs, L, L + Fe, L + SiO_2, and commercial Pt/C in O_2-saturated 0.1 mol L^{-1} KOH solution at a scan rate of 5 mV s^{-1} and rotation rate of 1600 rpm. (C) LSVs of LPCNs in O_2-saturated 0.1 mol L^{-1} KOH solution at various rotation speeds; scan rates, 5 mV s^{-1}. (D) Koutecky–Levich plot of LPCNs at different potentials. Parameters used for the calculation are presented in Supporting Information. Inset: the transferred electron number at different potentials.

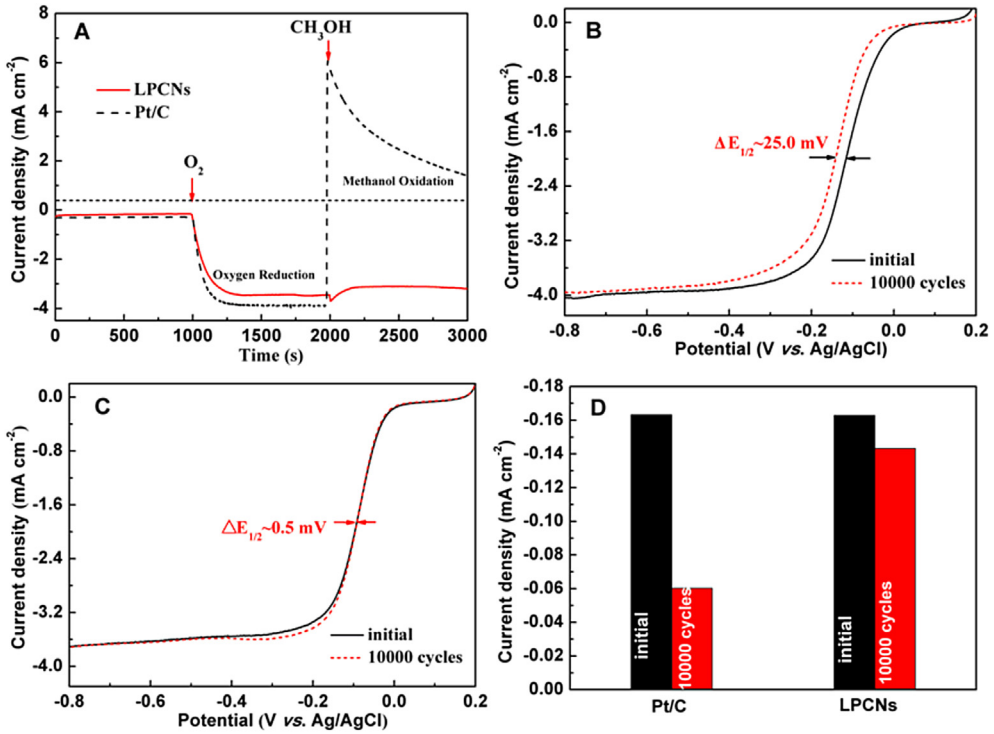

Fig. 4. (A) Current-time response of Pt/C and LPCNs at −0.26 V in 0.1 mol L^{-1} KOH solution saturated with N_2 (0–1000 s) or O_2 (1000–2000 s) and in O_2-saturated 3 mol L^{-1} CH_3OH (2000–3000). (B and C) LSVs of Pt/C and LPCNs before and after 10,000 cycles in O_2-saturated 0.1 mol L^{-1} KOH solution at a scan rate of 5 mV s^{-1} and rotation rate of 1600 rpm, respectively. (D) The current density of Pt/C and LPCNs at 0.09 V derived from the plots shown in Figure B and C.

glance, the curves show the differences. A flat plateau is observed for L + SiO_2 and LPCNs. L and L + Fe show a tilted plateau and a transition of control from kinetics to diffusion that is not as sharp as that of L + SiO_2 and LPCNs. As the previous discussion, in L + SiO_2 and LPCNs, the predominant pores are the mesopores, which are easily accessible to gaseous activation molecules, while, those of L and L + Fe are the micropores, which could restrict the O_2 diffusion limitation not only in the quiescent electrolyte layer close to the electrode but also inside the porous catalytic film [26]. Based on the above discussion, the difference of porous structures results in various shapes of curves of the as-prepared catalysts.

In Fig. 3B, L catalyst discloses a low ORR activity; −207 mV of the onset potential. Compared with L, L + Fe exhibits the positively shifted onset (−93 mV), clearly indicating a significant ORR activity enhancement by Fe doping. The enhanced ORR catalytic activity of L + Fe could be ascribed to the two factors, one is the doping Fe, which can increase the active sites by the formation of Fe–N bond. Another is the increase of the surface area (see Table S1), which can be favor of the mass transfer during the reaction process. Similarly, the promotion of SiO_2 template for catalytic activity is proved by the more positive onset potential (−33 mV) related to those of L, which could be related to the increase of the surface area derived from the SiO_2 template (see Table S1). After co-doped with Fe element and SiO_2 template, the onset potential on LPCNs electrode for ORR is ca. +20 mV, which is much higher than those of L, L + Fe, and L + SiO_2 electrodes, which is much larger than those of L, L + Fe, and L + SiO_2 electrodes. These results indicate the enhanced catalytic activity of LPCNs derived from the synergic effect between the doped-Fe and the mesoporous structure caused by the template SiO_2. Furthermore, the onset potential on LPCNs electrode is almost same as that of Pt/C electrode. Fig. 3B also shows an even more positive half-wave potential (ca. 28.3 mV) in LSV curves for LPCNs with respect to Pt/C electrode. The present performance of LPCNs indicates the superior catalytic activity of LPCNs towards ORR.

The LSVs from 400 to 2500 rpm were further performed to investigate the kinetics of electrochemical catalytic ORR at LPCNs electrode. LSVs for LPCNs in Fig. 3C show typical increasing current with higher rotations speeds. This result can be explained by shortened diffusion distance at high speeds, which is in accordance with other studies [27,28]. The corresponding Koutecky–Levich (K–L) plots that demonstrate the inverse current density as a function of the inverse of the square root of the rotation speed at different potential values are profiled in Fig. 3C. These K–L plots exhibit good linearity with parallelism, suggesting a first-order dependence of O_2 kinetics on LPCNs electrode [27]. According to the K–L equation (Supporting Information), the number of electrons transferred for ORR on LPCNs electrode is calculated, and the results are plotted as the inset in Fig. 3D. It can be observed that ORR on LPCNs electrode dominantly proceeds with the four-electron reaction pathway.

Catalysts for ORR require, a high catalytic selectivity for cathode reactions against fuel oxidation is important, because small organic molecule fuels, such as methanol, would poison the cathode catalyst once it cross over through the polymer electrolyte membrane from anode to cathode [13]. The methanol crossover effect for LPCNs and Pt/C was evaluated by the chronoamperometric responses to methanol introduced into an O_2-saturated electrolyte. The obtained results are profiled in Fig. 4A. A negative current appears when oxygen is introduced to N_2-saturated electrolyte at about 1000 s, indicating ORR occurs on both LPCNs and Pt/C electrodes. After adding a certain amount of methanol to the solution, the concentration of methanol is 3 mol L^{-1}, at about 2000 s, LPCNs retains stable current response, in contrast, the current on Pt/C electrode instantaneously reverse to positive value which is attributed to the methanol oxidation reaction occuring on Pt/C electrode. These results clearly show the excellent catalytic selectivity of LPCNs as a cathode catalyst for direct methanol fuel cells than the vulnerable Pt/C.

The preparation of LPCNs was also aimed at achieving high stability, which is of key importance in developing a real-world electrocatalyst. We adopted the electrochemical degradation tests of repeating potential cycles between 0.2 and −0.8 V in O_2-saturated 0.1 mol L^{-1} KOH solution. Fig. 4B–D shows LSVs of LPCNs and Pt/C before and after the stability test. It can be observed from Fig. 4B that Pt/C loses 10% in current density at 0.09 V, which is shown in Fig. 4D, after about 10000 cycles of potential cycling, which is accompanied by ca. 25.0 mV negative shift in the half-wave-potential of ORR polarization curve. LPCNs in Fig. 4C, however, exhibits only 1% decrease in current density at 0.09 V (see Fig. 4D) and 0.5 mV of negative shift for half-wave-potential in polarization curve. The good stability of LPCNs toward ORR may be attributed to its unique architecture and synergic effect between C, Fe, and N atoms.

4. Conclusions

In this work, we have described a programmed thermal reaction for the production of N-doped mesoporous carbon nanotube using lysine as nitrogen and carbon source, SiO_2 as the template. LPCNs show better catalytic activity than commercial Pt/C, which is attributed to the synergic effect between Fe, N-doping and the unique porous structure. Moreover, LPCNs also show high selectivity and stability compared to commercial Pt/C. These methods and mechanisms will provide valuable insight toward the development of N-doped mesoporous carbon nanotube catalysts with improved ORR activity and stability.

Acknowledgments

The authors would like to thank the National Natural Science Foundation of China (21163018, 21363022, and 51362027).

Appendix A. Supplementary data

Supplementary data related to this article can be found at http://dx.doi.org/10.1016/j.jpowsour.2014.06.156.

References

[1] R. Wang, H. Li, S. Ji, H. Wang, Z. Lei, Electrochim. Acta 55 (2010) 1519–1522.
[2] R. Wang, J. Jia, H. Wang, Q. Wang, S. Ji, Z. Tian, J. Solid State Electrochem. 17 (2013) 1021–1028.
[3] K. Wang, H. Wang, S. Ji, H. Feng, V. Linkov, R. Wang, RSC Adv. 3 (2013) 12039–12042.
[4] Y. Tang, B.L. Allen, D.R. Kauffman, A. Star, J. Am. Chem. Soc. 131 (2009) 13200–13201.
[5] R. Wang, T. Zhou, H. Li, H. Wang, H. Feng, J. Goh, S. Ji, J. Power Sources 261 (2014) 238–244.
[6] S. Wang, E. Iyyamperumal, A. Roy, Y. Xue, D. Yu, L. Dai, Angew. Chem. Int. Ed. 50 (2011) 11756–11760.
[7] L. Yang, S. Jiang, Y. Zhao, L. Zhu, S. Chen, X. Wang, Q. Wu, J. Ma, Y. Ma, Z. Hu, Angew. Chem. Int. Ed. 50 (2011) 7132–7135.
[8] Z. Liu, F. Peng, H. Wang, H. Yu, J. Tan, L. Zhu, Catal. Commun. 16 (2011) 35–38.
[9] A. Dorjgotov, J. Ok, Y. Jeon, S.-H. Yoon, Y. Shul, J. Appl. Electrochem. 43 (2013) 387–397.
[10] D. Yu, Q. Zhang, L. Dai, J. Am. Chem. Soc. 132 (2010) 15127–15129.
[11] W. Xiong, F. Du, Y. Liu, A. Perez, M. Supp, T.S. Ramakrishnan, L. Dai, L. Jiang, J. Am. Chem. Soc. 132 (2010) 15839–15841.
[12] W. Yang, T.-P. Fellinger, M. Antonietti, J. Am. Chem. Soc. 133 (2010) 206–209.
[13] J. Liang, Y. Zheng, J. Chen, J. Liu, D. Hulicova-Jurcakova, M. Jaroniec, S.Z. Qiao, Angew. Chem. Int. Ed. 51 (2012) 3892–3896.
[14] T. Zhou, H. Wang, K. Julian, S. Ji, V. Linkov, R. Wang, RSC Adv. 3 (2013) 16949–16953.
[15] Z. Jin, H. Nie, Z. Yang, J. Zhang, Z. Liu, X. Xu, S. Huang, Nanoscale 4 (2012) 6455–6460.

[16] T. Maiyalagan, B. Viswanathan, U.V. Varadaraju, Electrochem. Commun. 7 (2005) 905–912.
[17] R. Lv, T. Cui, M.S. Jun, Q. Zhang, A. Cao, D.S. Su, Z. Zhang, S.H. Yoon, J. Miyawaki, I. Mochida, F. Kang, Adv. Funct. Mater. 21 (2011) 999–1006.
[18] C.Y. Su, W.Y. Chu, Z.Y. Juang, K.F. Chen, B.M. Cheng, F.R. Chen, K.C. Leou, C.H. Tsai, J. Phys. Chem. C 113 (2009) 14732–14738.
[19] D. Geng, Y. Chen, Y. Chen, Y. Li, R. Li, X. Sun, S. Ye, S. Knights, Energy Environ. Sci. 4 (2011) 760–764.
[20] H. Yang, H. Li, H. Wang, S. Ji, J. Key, R. Wang, J. Electrochem. Soc. 161 (2014) F795–F802.
[21] H. Yang, H. Wang, S. Ji, V. Linkov, R. Wang, Int. J. Hydrogen Energy 39 (2014) 3739–3745.
[22] C.H. Choi, S.H. Park, S.I. Woo, ACS Nano 6 (2012) 7084–7091.
[23] Y. Tan, C. Xu, G. Chen, X. Fang, N. Zheng, Q. Xie, Adv. Funct. Mater. 22 (2012) 4584–4591.
[24] J. Liang, Y. Jiao, M. Jaroniec, S.Z. Qiao, Angew. Chem. Int. Ed. 51 (2012) 1–6.
[25] K. Gong, F. Du, Z. Xia, M. Durstock, L. Dai, Science 323 (2009) 760–764.
[26] F.d.r. Jaouen, J. Herranz, M. Lefevre, J.-P. Dodelet, U.I. Kramm, I. Herrmann, P. Bogdanoff, J. Maruyama, T. Nagaoka, A. Garsuch, J.R. Dahn, T. Olson, S. Pylypenko, P. Atanassov, E.A. Ustinov, ACS Appl. Mater. Interfaces 1 (2009) 1623–1639.
[27] Z. Wen, S. Ci, F. Zhang, X. Feng, S. Cui, S. Mao, S. Luo, Z. He, J. Chen, Adv. Mater. 24 (2012) 1399–1404.
[28] R. Liu, D. Wu, X. Feng, K. Müllen, Angew. Chem. Int. Ed. 49 (2010) 2565–2569.